

# All-fiber upconversion high spectral resolution wind lidar using a Fabry-Perot interferometer

MINGJIA SHANGGUAN,<sup>1,2,3</sup> HAIYUN XIA,<sup>1,3,4</sup> CHONG WANG,<sup>1</sup> JIAWEI QIU,<sup>1</sup> GUOLIANG SHENTU,<sup>2,5</sup> QIANG ZHANG,<sup>2,5,6</sup> XIANKANG DOU,<sup>1,\*</sup> AND JIAN-WEI PAN<sup>2,5</sup>

<sup>1</sup>CAS Key Laboratory of Geospace Environment, USTC, Hefei, 230026, China

<sup>2</sup>Shanghai Branch, National Laboratory for Physical Sciences at Microscale and Department of Modern Physics, USTC, Shanghai, 201315, China

<sup>3</sup>These authors contributed equally to this work

<sup>4</sup>Collaborative Innovation Center of Astronautical Science and Technology, HIT, Harbin 150001, China

<sup>5</sup>Synergetic Innovation Center of Quantum Information and Quantum Physics, USTC, Hefei 230026, China

<sup>6</sup>Jinan Institute of Quantum Technology, Jinan, Shandong 250101, China

\*dou@ustc.edu.cn

**Abstract:** An all-fiber, micro-pulse and eye-safe high spectral resolution wind lidar (HSRWL) at 1.5  $\mu\text{m}$  is proposed and demonstrated by using a pair of upconversion single-photon detectors and a fiber Fabry-Perot scanning interferometer (FFP-SI). In order to improve the optical detection efficiency, both the transmission spectrum and the reflection spectrum of the FFP-SI are used for spectral analyses of the aerosol backscatter and the reference laser pulse. Taking advantages of high signal-to-noise ratio of the detectors and high spectral resolution of the FFP-SI, the center frequencies and the bandwidths of spectra of the aerosol backscatter are obtained simultaneously. Continuous LOS wind observations are carried out on two days at Hefei (31.843 °N, 117.265 °E), China. The horizontal detection range of 4 km is realized with temporal resolution of 1 minute. The spatial resolution is switched from 30 m to 60 m at distance of 1.8 km. In a comparison experiment, LOS wind measurements from the HSRWL show good agreement with the results from an ultrasonic wind sensor (Vaisala windcap WMT52). An empirical method is adopted to evaluate the precision of the measurements. The standard deviation of the wind speed is 0.76 m/s at 1.8 km. The standard deviation of bandwidth variation is 2.07 MHz at 1.8 km.

©2016 Optical Society of America

**OCIS codes:** (010.3640) Lidar; (010.0280) Remote sensing and sensors; (190.7220) Upconversion; (280.3340) Laser Doppler velocimetry.

## References and links

1. C. J. Grund, R. M. Banta, J. L. George, J. N. Howell, M. J. Post, R. A. Richter, and A. M. Weickmann, "High-resolution Doppler lidar for boundary layer and cloud research," *J. Atmos. Ocean. Technol.* **18**(3), 376–393 (2001).
2. N. S. Prasad, A. Tracy, S. Vitorino, R. Higgins, and R. Sibell, "Innovative fiber-laser architecture-based compact wind lidar," *Proc. SPIE* **9754**, 97540J (2016).
3. W. L. Eberhard, R. E. Cupp, and K. R. Healy, "Doppler lidar measurement of profiles of turbulence and momentum flux," *J. Atmos. Ocean. Technol.* **6**(5), 809–819 (1989).
4. I. N. Smalikho, F. Köpp, and S. Rahm, "Measurement of atmospheric turbulence by 2- $\mu\text{m}$  Doppler lidar," *J. Atmos. Ocean. Technol.* **22**(11), 1733–1747 (2005).
5. S. C. Tucker, C. J. Senff, A. M. Weickmann, W. A. Brewer, R. M. Banta, S. P. Sandberg, D. C. Law, and R. M. Hardesty, "Doppler lidar estimation of mixing height using turbulence, shear and aerosol profiles," *J. Atmos. Ocean. Technol.* **26**(4), 673–688 (2009).
6. H. Shimizu, K. Noguchi, and C. Y. She, "Atmospheric temperature measurement by a high spectral resolution lidar," *Appl. Opt.* **25**(9), 1460–1466 (1986).
7. Z. Liu, I. Matsui, and N. Sugimoto, "High-spectral-resolution lidar using an iodine absorption filter for atmospheric measurements," *Opt. Eng.* **38**(10), 1661–1670 (1999).
8. D. Hua, M. Uchida, and T. Kobayashi, "Ultraviolet Rayleigh-Mie lidar for daytime-temperature profiling of the troposphere," *Appl. Opt.* **44**(7), 1315–1322 (2005).

9. B. Witschas, C. Lemmerz, and O. Reitebuch, "Daytime measurements of atmospheric temperature profiles (2-15 km) by lidar utilizing Rayleigh-Brillouin scattering," *Opt. Lett.* **39**(7), 1972–1975 (2014).
10. H. Xia, X. Dou, M. Shangguan, R. Zhao, D. Sun, C. Wang, J. Qiu, Z. Shu, X. Xue, Y. Han, and Y. Han, "Stratospheric temperature measurement with scanning Fabry-Perot interferometer for wind retrieval from mobile Rayleigh Doppler lidar," *Opt. Express* **22**(18), 21775–21789 (2014).
11. W. Huang, X. Chu, J. Wiig, B. Tan, C. Yamashita, T. Yuan, J. Yue, S. D. Harrell, C. Y. She, B. P. Williams, J. S. Friedman, and R. M. Hardesty, "Field demonstration of simultaneous wind and temperature measurements from 5 to 50 km with a Na double-edge magneto-optic filter in a multi-frequency Doppler lidar," *Opt. Lett.* **34**(10), 1552–1554 (2009).
12. Z. Cheng, D. Liu, J. Luo, Y. Yang, Y. Zhou, Y. Zhang, L. Duan, L. Su, L. Yang, Y. Shen, K. Wang, and J. Bai, "Field-widened Michelson interferometer for spectral discrimination in high-spectral-resolution lidar: theoretical framework," *Opt. Express* **23**(9), 12117–12134 (2015).
13. C. Weitkamp, *LIDAR Range-Resolved Optical Remote Sensing of the Atmosphere* (Springer, 2006).
14. H. Xia, X. Dou, D. Sun, Z. Shu, X. Xue, Y. Han, D. Hu, Y. Han, and T. Cheng, "Mid-altitude wind measurements with mobile Rayleigh Doppler lidar incorporating system-level optical frequency control method," *Opt. Express* **20**(14), 15286–15300 (2012).
15. M. Harris, G. N. Pearson, J. M. Vaughan, D. Letalick, and C. J. Karlsson, "The role of laser coherence length in continuous-wave coherent laser radar," *J. Mod. Opt.* **45**(8), 1567–1581 (1998).
16. M. J. McGill and J. D. Spinhirne, "Comparison of two direct-detection Doppler lidar techniques," *Opt. Eng.* **37**(10), 2675–2686 (1998).
17. H. Xia, D. Sun, Y. Yang, F. Shen, J. Dong, and T. Kobayashi, "Fabry-Perot interferometer based Mie Doppler lidar for low tropospheric wind observation," *Appl. Opt.* **46**(29), 7120–7131 (2007).
18. C. Souprayen, A. Garnier, A. Hertzog, A. Hauchecorne, and J. Porteneuve, "Rayleigh-Mie Doppler wind lidar for atmospheric measurements. I. Instrumental setup, validation, and first climatological results," *Appl. Opt.* **38**(12), 2410–2421 (1999).
19. O. Reitebuch, C. Lemmerz, E. Nagel, U. Paffrath, Y. Durand, M. Endemann, F. Fabre, and M. Chaloupy, "The airborne demonstrator for the direct-detection Doppler wind lidar ALADIN on ADM-Aeolus. Part I: Instrument design and comparison to satellite instrument," *J. Atmos. Ocean. Technol.* **26**(12), 2501–2515 (2009).
20. American National Standards Institute, American National Standard for the Safe Use of Lasers z136.1 (American National Standards Institute, 2007).
21. C. L. Korb, B. M. Gentry, and C. Y. Weng, "Edge technique: theory and application to the lidar measurement of atmospheric wind," *Appl. Opt.* **31**(21), 4202–4213 (1992).
22. H. Xia, G. Shentu, M. Shangguan, X. Xia, X. Jia, C. Wang, J. Zhang, J. S. Pelc, M. M. Fejer, Q. Zhang, X. Dou, and J. W. Pan, "Long-range micro-pulse aerosol lidar at 1.5  $\mu\text{m}$  with an upconversion single-photon detector," *Opt. Lett.* **40**(7), 1579–1582 (2015).
23. L. Høgstvedt, A. Fix, M. Wirth, C. Pedersen, and P. Tidemand-Lichtenberg, "Upconversion-based lidar measurements of atmospheric CO<sub>2</sub>," *Opt. Express* **24**(5), 5152–5161 (2016).
24. P. J. Rodrigo and C. Pedersen, "Monostatic coaxial 1.5  $\mu\text{m}$  laser Doppler velocimeter using a scanning Fabry-Perot interferometer," *Opt. Express* **21**(18), 21105–21112 (2013).
25. P. J. Rodrigo and C. Pedersen, "Direct detection doppler lidar using a scanning fabry-perot interferometer and a single-photon counting module," in *The European Conference on Lasers and Electro-Optics*, (Optical Society of America, 2015), paper CH\_P\_15.
26. E. Diamanti, C. Langrock, M. M. Fejer, Y. Yamamoto, and H. Takesue, "1.5  $\mu\text{m}$  photon-counting optical time-domain reflectometry with a single-photon detector based on upconversion in a periodically poled lithium niobate waveguide," *Opt. Lett.* **31**(6), 727–729 (2006).
27. H. Venghaus, *Wavelength Filters in Fibre Optics* (Springer, 2006).
28. L. Xin, C. Xuewu, L. Faquan, Y. Yong, W. Kuijun, L. Yajuan, X. Yuan, and G. Shunsheng, "Temperature-insensitive laser frequency stabilization to molecular absorption edge using an acousto-optic modulator," *Opt. Lett.* **39**(15), 4416–4419 (2014).
29. G. L. Shentu, J. S. Pelc, X. D. Wang, Q. C. Sun, M. Y. Zheng, M. M. Fejer, Q. Zhang, and J. W. Pan, "Ultralow noise up-conversion detector and spectrometer for the telecom band," *Opt. Express* **21**(12), 13986–13991 (2013).

## 1. Introduction

Doppler wind lidars (DWL) have shown their efficacy in the remote measurement of spatially resolved atmospheric wind velocities in many applications, including dynamic property of the atmospheric boundary layer [1], aircraft wake vortices [2], air turbulence [3, 4] and wind shear [5]. With high spectral resolution techniques, atmospheric properties (temperature, wind or other aerosol optical parameters) can be determined using high-resolution frequency discriminators, such as atomic vapor filter [6], iodine absorption filter [7], Fabry-Perot interferometer [8–10], Na double-edge magneto-optic filter [11], and Michelson interferometer [12]. The measurement principle of the DWL relies on the detection of the radial Doppler shift carried on atmospheric aerosol or molecular backscatter. The DWL is generally classified into two main categories: the coherent (heterodyne)

detection lidar (CDL) and the direct detection lidar (DDL) [13]. Heterodyne detection is adopted in the CDL, where the atmospheric backscatter is mixed with a local oscillator optically. The Doppler shift of the beating RF signal is in proportion to the LOS wind velocity. CDL has matured over the past few decades, with compact operational systems using eye-safe and solid-state lasers commercially available. The sensitivity of CDL is high since local oscillator amplifies the weak aerosol backscatter. And, it is less sensitive to background light. In the DDL, no local oscillator but the optical frequency discriminator is used to convert the Doppler shift into an irradiance variation. DDL can detect wind speed from either the narrow-band aerosol backscatter or the spectrally broadened molecular backscatter. In comparison, CDL has low sensitivity to the broad-band molecular backscatter; it can only detect wind based on aerosol backscatter [10, 14].

Although the CDL achieved great success in different applications, there are still some challenges in developing a CDL with spatial resolution of meter-level. Firstly, high frequency sampling is required to improve the spatial resolution of coherent lidars, resulting a heavy burden in real-time processing of the raw signal. For example, 750MHz sampling rate and 8-bit analog-to-digital resolution is used to achieve a range resolution of 15 m. Redundant arrays of independent disks with 24-TB size are used to save the raw data, and post-processing is adopted [2]. Secondly, the coherent system is strongly affected by shot noise, phase noise and the relative intensity noise of the local oscillator. Thirdly, the remote sensing range is limited by the laser coherence length [15]. Finally, in order to distinguish the sign of the Doppler shift, acousto-optic modulator must be adopted as the frequency shifter.

In comparison, the DDL has several advantages including having large remote sensing range, inherent sign discrimination of Doppler shift, more robust to phase aberration, much simpler data acquisition and data processing. However, in the DDL, frequency locking of the Doppler shift discriminator to the working laser with high precision (less than 1 MHz) is required, making the system complicated. According to different implementations, the direct detection techniques fall into two types. The first one is edge technique, in which one or more narrowband filters are used and the Doppler frequency shift is determined from the variation of the transmitted signal strength through the filter. The other is called fringe-imaging technique, where the Doppler shift is determined from the radial angular distribution or spatial movement of the interference patterns through an interferometer. By using imaging technique, spectral changes (including both the Doppler shift and frequency broadening) can be detected. The two implementations have been compared theoretically [16].

In this work, a new high spectral resolution wind lidar (HSRWL) at 1.5  $\mu\text{m}$  is proposed, where spectra of aerosol backscatter along the line-of-sight of the telescope are analyzed by using a fiber Fabry-Perot interferometer and detected with two upconversion detectors. By applying direct spectral analyses, the frequency shift and the bandwidth broadening of these spectra are retrieved simultaneously. The Doppler shifts are determined by calculating the difference in center frequencies of the aerosol backscatter and the reference signal.

In many applications, eye safety, long-range sensing capability and large dynamic range of the wind speed measurement are the primary considerations in Doppler wind lidar design. Direct-detection Doppler lidars usually operate at wavelength of 1.064  $\mu\text{m}$  [17], 0.532  $\mu\text{m}$  [18] or 0.355  $\mu\text{m}$  [14, 19], using the fundamental, second or third harmonics of an Nd: YAG laser. The proposed lidar operates at 1.5  $\mu\text{m}$ , the standard wavelength of telecommunications industry, providing many advantages. Firstly, the 1.5 $\mu\text{m}$  lasers permit the highest maximum permissible exposure to human eyes in the optical spectrum from 0.3  $\mu\text{m}$  to 10  $\mu\text{m}$  [20]. Secondly, optical fiber components and devices developed for optical communications are commercial available. Thirdly, components have been designed to be environmentally hardened, making the system highly reliable. In addition, the advantages of the longer wavelength include: lower requirement on optical surface quality and higher immunity to atmospheric refractive turbulence.

The measurement dynamic range of wind speed is a significant issue, for example the wind speed can reach as large as 60 m/s in the stratosphere [14]. In the proposed HSRWL system, the wind speed dynamic range is determined by the free spectral range (FSR) of the

FFP-SI, and is typically larger than that of the DDL based on edge technique, where the dynamic range is determined by the bandwidth of the Fabry-Perot interferometer in the single-edge scheme [21] or by the spacing (spectral difference) between the two FPI channels in the double-edge scheme [14]. In the CDL, the dynamic range is limited by the bandwidth of the detectors and the ADC. Large dynamic measurement requires detectors with broader bandwidth and ADC with faster sampling speed, in order to meet the Nyquist criterion.

In comparison, the lidar system based on the fringe-imaging technique is found to have large measurement dynamic range [16], similar to the proposed HSRWL. However, an intrinsic property of the fringe-imaging is the requirement of a multi-pixel charge coupled device that is matched to the pattern of the FPI or the Michelson interferometer. This results in a detector package that can be more complicated than the single-pixel detector used in the HSRWL.

In our previous work, a temperature lidar [10] and Doppler wind lidars [14, 17] based on free-space Fabry-Perot interferometer and photon-counting detectors have been demonstrated. However, it is hard to eliminate the parallelism error of the reflecting mirrors during the cavity scanning and the mode-dependent spectral broadening due to its illuminating condition. In this work, this problem is solved by using a lensless FFP-SI.

In contrast to our previous aerosol lidar at 1.5  $\mu\text{m}$  [22], the HSRWL adopts upconversion detectors with all-fiber configuration. Recently, an intracavity upconversion system has been demonstrated for detection of atmospheric  $\text{CO}_2$  [23]. A Doppler velocimetry has been demonstrated before by using a scanning Fabry-Perot interferometer and an InGaAs photodetector [24, 25]. Although InGaAs detector is commercial available, its high after-pulse probability distorts the raw signal significantly and the time gating operation mode exhibits periodic blind zones [26].

## 2. Principle

The key instrument inside the optical receiver of the HSRWL is a FFP-SI. The cavity of the FFP-SI is formed by two highly reflective multilayer mirrors that are deposited directly onto two carefully aligned fiber ends [27]. The anti-reflection coated fiber inserted in the cavity provides confined light-guiding and eliminates secondary cavity. Due to the fiber-based design, the insertion loss is low to be 0.3 dB. Here, a stacked piezoelectric transducer (PZT) is used to axially strain the single-mode fiber inserted in the cavity. Frequency scanning of the FFP-SI is achieved by scanning the cavity length [17]. A step change of the cavity  $\Delta l$  is related to the frequency sampling interval  $\Delta\nu$  as

$$\Delta\nu/\nu_0 = -\Delta l/l, \quad (1)$$

where,  $l = 25.59$  mm is the cavity spacing,  $\nu_0$  is the frequency of the incident laser. As an example, if one needs to increase the frequency of FFP-SI over 4.02 GHz, the cavity spacing should be shrunk 532 nm. Note that, according to the definition of the FSR =  $c/2nl$  ( $c$  is vacuum speed of light,  $n$  is the index of the fiber core, and  $l$  is the cavity spacing), the FSR is inversely proportional to  $l$ . According to Eq. (1), if the cavity spacing  $l$  shrinks 4.02 GHz, the FSR of the FPI-SI will increase 0.08 MHz, which is ignorable.

An HSRWL using the FFP-SI is proposed, in which both the transmission spectrum and the reflection spectrum of the backscatter on the FFP-SI are used for spectral analyses. As shown in Fig. 1(a), in a calibration experiment, a continuous-wave (CW) monochromatic laser is used. By changing the voltage fed to the PZT, the transmission spectra and the reflection spectra are recorded simultaneously using an oscilloscope. In the frequency domain, the transmission and reflection of a Fabry-Perot interferometer is periodic with a constant FSR. In a calibration process, a broadband light from an amplified spontaneous emission (ASE) source is fed to the FFP-SI without voltage added to the PZT, and the FSR is read out to be 4.02 GHz directly from an optical spectrum analyzer (Yokogawa, AQ6370C). In Fig. 1, a time to frequency conversion is performed by using the FSR of 4.02 GHz. If the

FFP-SI analyzes both aerosol backscatter and the reference laser, the Doppler shift will move the spectra of aerosol backscatter to one side of the reference peak. The red-shifted or blue-shifted determine the sign of the Doppler shift. Then, the possible dynamic range of velocity measurement spans from  $-1/2$  FSR to  $1/2$  FSR. Taking the FSR of the FFP-SI is 4.02 GHz, the maximum wind speed dynamic range of the proposed HSRWL is span from  $-1557$  m/s to  $+1557$  m/s at 1550 nm.

Note that, given a constant scanning step, the wider the scanning range, the longer time it takes. For atmospheric boundary layer application, the dynamic range of wind speed is  $\pm 35$  m/s, indicating a Doppler range of  $\pm 45.15$  MHz. Considering the FWHM of the transmission of aerosol through the FPI, the suggested scanning range is 300 MHz in this work.

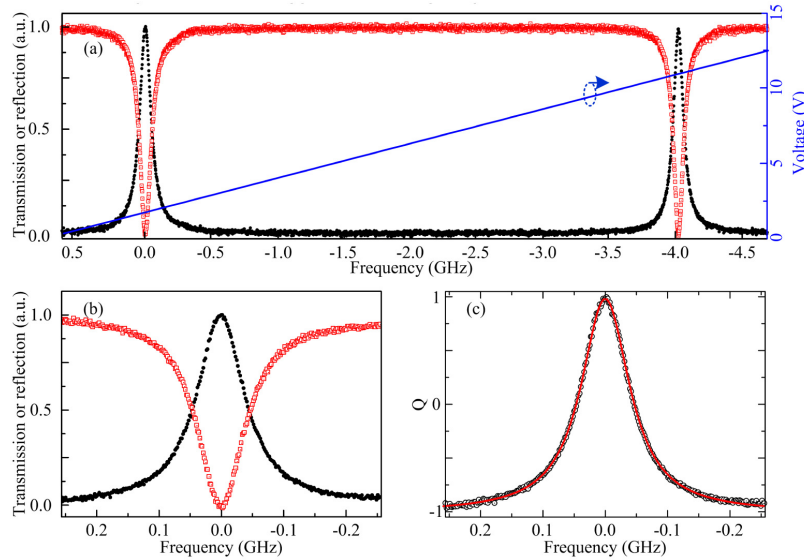


Fig. 1. (a) Transmission spectrum (circles) and reflection spectrum (squares) of the monochromatic CW laser through the FFP-SI as the driven voltage increases from 0.3 V to 12.5 V, (b) Zoom-in image of Fig. 1(a), (c) The calculated Q function (circles) and its Lorentzian fitting result (solid line).

In order to retrieve the Doppler shift, spectral analyses is performed as follows. For the pulsed laser, the measured transmission spectrum of the aerosol backscatter  $T(v, v_c, v_D, \Delta v_M)$  is the convolution of the spectrum of aerosol backscatter  $I(v, v_c, v_D, \Delta v_M)$  and the transmission function of the FFP-SI  $h(v)$ :

$$T(v, v_c, v_D, \Delta v_M) = h(v) * I(v, v_c, v_D, \Delta v_M), \quad (2)$$

where  $*$  denotes the convolution,  $v$  is the optical frequency relative to the center of the spectrum of the reference signal,  $v_c$  is the center frequency of the spectrum of the reference signal,  $v_D$  is the Doppler shift carried on atmospheric backscatter,  $\Delta v_M$  is the half-width at the  $1/e$  intensity level of the spectrum of aerosol backscatter.

The FFP-SI is fabricated with single-mode fiber with a negligible divergence in the cavity, thus its transmission is approximated to a Lorentzian function:

$$h(v) = T_0 / \left[ 1 + (v)^2 / (\Delta v_{FPI} / 2)^2 \right], \quad (3)$$

where  $\Delta v_{FPI}$  is the full width at half maximum of the transfer function,  $T_0$  is the maximum transmission factor given by

$$T_0 = a_t(1-r_f)^2 / (1-a_t \cdot r_f)^2, \quad (4)$$

Where  $a_t$  is the attenuation factor,  $r_f$  is the reflection coefficient of the reflecting ends. Since the Brownian motion of aerosol particles does not broaden the spectrum significantly, the spectrum of aerosol backscatter  $I(v, v_c, v_D, \Delta v_M)$  has nearly the same shape as the spectrum of the outgoing laser pulse. Thus, the spectrum of aerosol backscatter can be approximated by a Gaussian function:

$$I(v, v_c, v_D, \Delta v_M) = (\sqrt{\pi} \Delta v_M)^{-1} \exp\left[-(v-v_c-v_D)^2 / \Delta v_M^2\right], \quad (5)$$

Similarly, the measured reflection spectrum  $R(v, v_c, v_D, \Delta v_M)$  can be expressed as follow:

$$R(v, v_c, v_D, \Delta v_M) = r(v) * I(v, v_c, v_D, \Delta v_M), \quad (6)$$

where  $r(v) = 1-h(v)$  is the reflection function of the FFP-SI. Then, a frequency response function Q is normalized and defined as

$$Q(v, v_c, v_D, \Delta v_M) = \frac{a^* \cdot T(v, v_c, v_D, \Delta v_M) - R(v, v_c, v_D, \Delta v_M)}{a^* \cdot T(v, v_c, v_D, \Delta v_M) + R(v, v_c, v_D, \Delta v_M)}, \quad (7)$$

where  $a^*$  is a system constant, which can be determined in the calibration. By applying a least squares fit procedure to the Q function, the center frequency  $v_c$  and the bandwidth  $\Delta v_M$  can be retrieved simultaneously. The performance of the FFP-SI is characterized by spectrally analyzing the result from the Fig. 1(a). Since the linewidth of the monochromatic CW laser ( $\sim 3$  kHz) is much less than that of the  $\Delta v_{FPI}$  ( $\sim 94$  MHz), the measured spectrum represents the feature of the FFP-SI. Using the measured data near the first resonance peak as shown in Fig. 1(b), the frequency response function Q can be calculated by using Eq. (7). The calculated Q function and fitting result are presented in Fig. 1(c). The fitted  $\Delta v_{FPI}$  is 94 MHz. In this calibration experiment, the overall transmission efficiency and reflection efficiency of the FFP-SI are measured to be 30% and 58% respectively.

In construct to the CDL, the HSRWL has several advantages as mentioned in the introduction. However, the HSRWL has also several technical challenges, which are not present in its coherent counterpart. For weak backscatter from the aerosol, detection with high signal-to-noise ratio is required. To address this challenge, upconversion detectors with high quantum efficiency and low dark-count noise are adopted, which convert the working wavelength from 1548 nm to 863 nm and then detect with Si-APDs. In addition, the frequency stability control of the frequency discriminator is also a challenging task [14, 28]. Here, the frequency drift of the FFP-SI relative to the outgoing laser is controlled by putting the interferometer inside a chamber.

### 3. Instrument

A schematic diagram of the HSRWL is shown as Fig. 2. A continuous wave from a seed laser (Keyopsys, PEFL-EOLA) is chopped into pulse train after passing through an electro-optic modulator (EOM) (Photline, MXER-LN). The EOM is driven by a pulse generator (PG), which determines the shape and pulse repetition rate (12 kHz) of the laser pulse. A small fraction of the pulse laser is split out as a reference signal by using a polarization-maintaining fiber splitter. The reference signal is attenuated to the single-photon level by using a variable attenuator (VA<sub>0</sub>) and then fed to the optical receiver. The main laser pulse from the other output of the splitter is fed to an erbium-doped fiber amplifier (Keyopsys, PEFA-EOLA), which delivers pulse train with pulse energy of 50  $\mu$ J and pulse duration of 200 ns. A large mode area fiber is used to increase the threshold of stimulated Brillouin scattering (SBS) and self-saturation of amplified spontaneous emission (ASE). The pulsed laser beam is collimated

and transmitted to the atmosphere by an off-axis telescope with diameter of 80 mm. The outgoing laser and atmospheric backscatter are separated by an optical switch composed of a quarter-wave plate and a polarizing beam splitter (PBS).

An optical circulator is used to separate the transmitted signal and the reflected signal from the FFP-SI. The FFP-SI is made of single-mode fiber, thus two polarization controllers are added at the front and rear ends of the FFP-SI to eliminate the polarization dependent loss. The continuous wave from the pump laser at 1950 nm is followed by a thulium-doped fiber amplifier (TDFA), both manufactured by AdValue Photonics (Tucson, AZ). The residual ASE noise is suppressed by using a 1.55  $\mu\text{m}$ /1.95  $\mu\text{m}$  wavelength division multiplexer (WDM<sub>1</sub>). The pump laser is split into two beams by a 3 dB fiber splitter, one used for the transmitted signal and the other for the reflected signal. The reflected backscatter signal and the pump laser are coupled into a periodically poled Lithium niobate waveguide (PPLN-W<sub>1</sub>) via the WDM<sub>1</sub>. In the same way, the transmitted backscatter signal and the pump laser are coupled into a PPLN-W<sub>2</sub> via the WDM<sub>2</sub>. Optimized quasi-phase matching condition is achieved by tuning the temperature of the PPLN-W with a thermoelectric cooler [29]. Here, the upconversion detectors are integrated into two all-fiber modules, in which the PPLN-Ws are coupled into polarization-maintaining fiber/multimode fiber (MMF) at the front/rear end. The backscatter photons at 1548 nm are converted into sum-frequency photons at 863 nm and then picked out from the pump and spurious noise by using an interferometer filter (IF) at 863 nm with 1nm bandwidth. Finally, the photons at 863 nm are detected by using Si-APDs (EXCELITAS). The TTL signals corresponding to the received photons are recorded on a multiscaler (FAST ComTec, MCS6A) and then transferred to a computer. The system detection efficiency of the upconversion detector used to detect the transmitted signal is tuned to 20.5% with a noise level of 300 Hz. For another upconversion detector, the system detection efficiency is tuned to 15% with a noise level of 330 Hz.

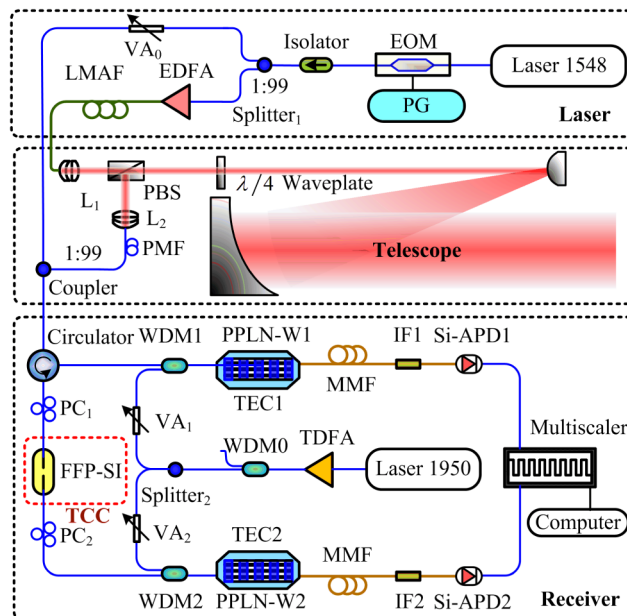


Fig. 2. Optical layout of the system. EOM, electro-optic modulator; PG, pulse generator; VA, variable attenuator; EDFA, erbium doped fiber amplifier; LMAF, large-mode-area fiber; PBS, polarizing beam splitter; PMF, polarization-maintaining fiber; PC, polarization controller; TCC, temperature controlled chamber; FFP-SI, fiber Fabry-Perot scanning interferometer; TDFA, thulium doped fiber amplifier; WDM, wavelength division multiplexer; PPLN-W, periodically poled Lithium niobate waveguide, MMF, multimode fiber; TEC, thermoelectric cooler; IF, interferometer filter.

It is useful to understand how the different signals are detected through a data acquisition timing sequence, as shown in Fig. 3. A synchronization transistor-transistor logic (TTL) output from the PG is applied to synchronize the range-gating electronics. The signal collected in ten bins before the laser pulse is used to measure the averaging background. The reference signal from the  $VA_0$  is collected in the three bins. The output of the Si-APD is disabled when a low level of TTL is applied to its gate input. Hence the trigger to the Si-APDs can be used to eliminate the strong mirror reflections from the telescope. The atmospheric backscatter signal is delayed by a PMF of 160 m to avoid mixing with the reference signal.

It is indispensable to control the temperature of the FFP-SI precisely, due to its temperature-sensitive characteristics. In this work, the FFP-SI is cased in a chamber, and two-stage temperature controller is applied. Temperature of the chamber is controlled by using Peltier elements with a PID temperature controller (BelektroniG B-20).

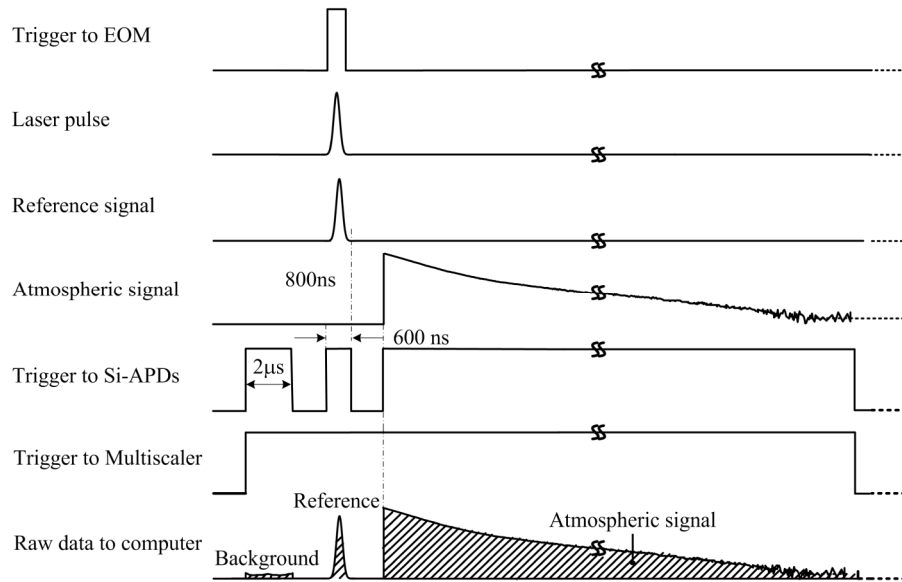


Fig. 3. Timing sequence of data acquisition for a single laser pulse.



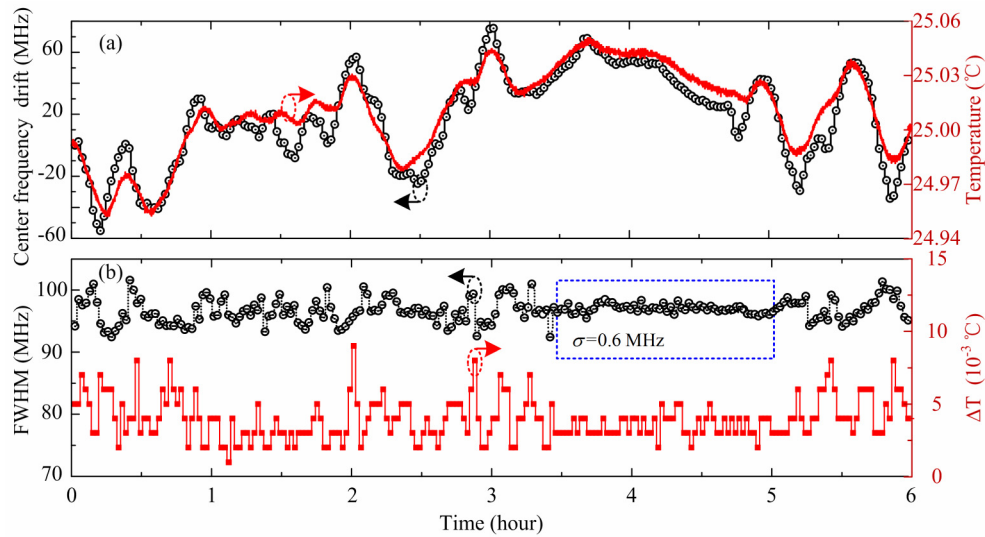


Fig. 4. (a) Frequency drift and (b) bandwidth change of the FFP-SI due to temperature fluctuation.

In order to investigate the effect of the temperature drift on measurement, the inner controller is shut down, and the frequency response function is measured by scanning the cavity length with the reference laser pulse over 95 seconds. By applying a least-square fit procedure to the measured frequency response functions, the center frequencies and bandwidths are retrieved simultaneously. As shown in Fig. 4(a), the center frequencies (circles) and temperature drift (line) are monitored over 6 hours.

Obviously, the temperature of the FFP-SI fluctuates as shown in Fig. 4, even the ambient temperature inside the lab is  $25 \pm 1 \text{ }^\circ\text{C}$ . Also the bandwidth change between two scanning steps is plotted along with the temperature change ( $\Delta T$ ), as shown in Fig. 4(b). One can see that large temperature drifts will seriously affect the accuracy of the bandwidth measurement. Fortunately, the standard deviation of the bandwidth change is 0.6 MHz when the temperature drift is within  $\pm 0.002 \text{ }^\circ\text{C}$ . When the inner PID control of the temperature is turned on, a stability of  $\pm 0.001 \text{ }^\circ\text{C}$  is realized in 1 minute, as shown in Fig. 5. Consequently, the system error induced by the temperature fluctuation can be ignored when the temperature controller is used. In this work, the frequency drift of the seed laser is controlled within 0.1 MHz per minute. And the pulse shape of the outgoing laser is defined accurately by using the EOM. All these characteristics of this DDL guarantee the precision of the measurements.

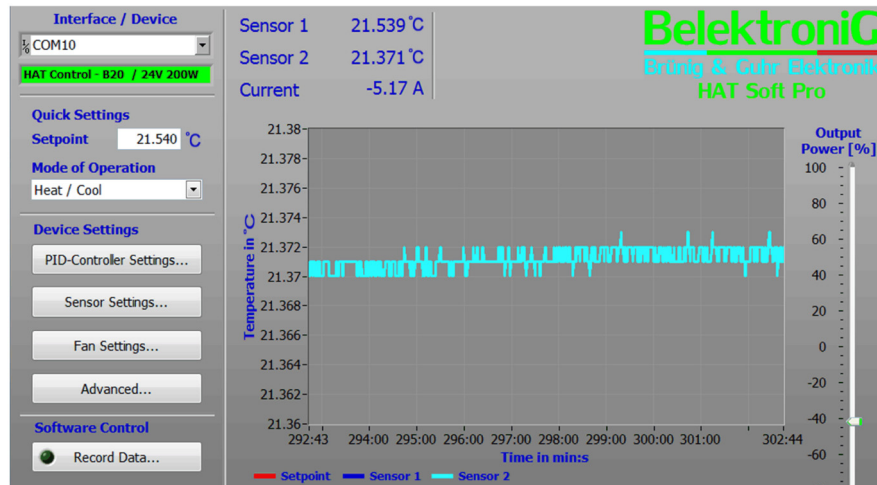


Fig. 5. Graphical user interface of the temperature controller (temperature stability of  $\pm 0.001$  °C in one minutes is realized)

#### 4. Field experiments

Wind detection is carried out at Hefei (31.83 °N, 117.25 °E) in Anhui province, China. The location is 29.8 m above the sea level.

In order to obtain the aerosol backscatter spectra, the FFP-SI is scanned over 39.30 nm /297 MHz with a step of 1.31 nm / 9.9 MHz, by changing the driven voltage. At each step, backscatters of 22000 laser pulses are accumulated. Taking the time for data processing into account, each step costs 2 seconds. Considering 30 steps, the sampling of the entire aerosol backscatter spectra takes 1 minute. An example is shown in Fig. 6, both the transmitted spectra and the reflected spectra of the backscatter at different distance are recorded.

Then the corresponding Q functions are calculated. An example of the calculated Q functions of backscatter at 0.03 km and 1.80 km are shown in Fig. 7(a), and the corresponding fitting results are plotted with lines. The fitting residuals are plotted in Fig. 7(b). Profiles of transmitted and reflected backscatter along the distance indicate the quality of the measured data. As shown in Fig. 7(c), backscatter profiles at different frequencies are plotted. Judging from the raw signal, one can see that the detection range of 4 km can be reached.

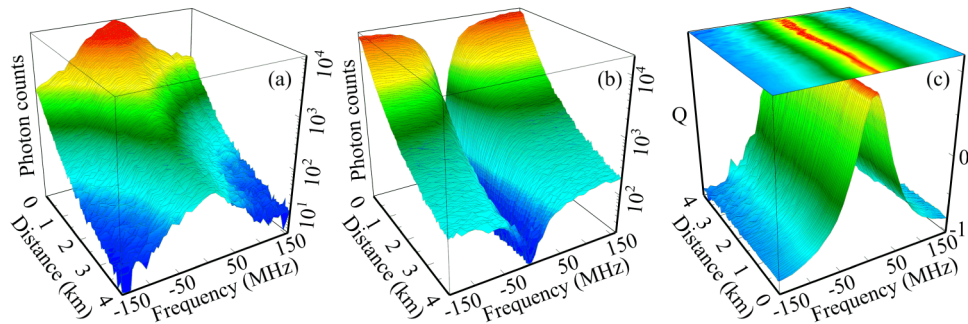


Fig. 6. Photon counts of transmitted backscatter signal (a), reflected backscatter signal (b) and the corresponding frequency response functions (c).

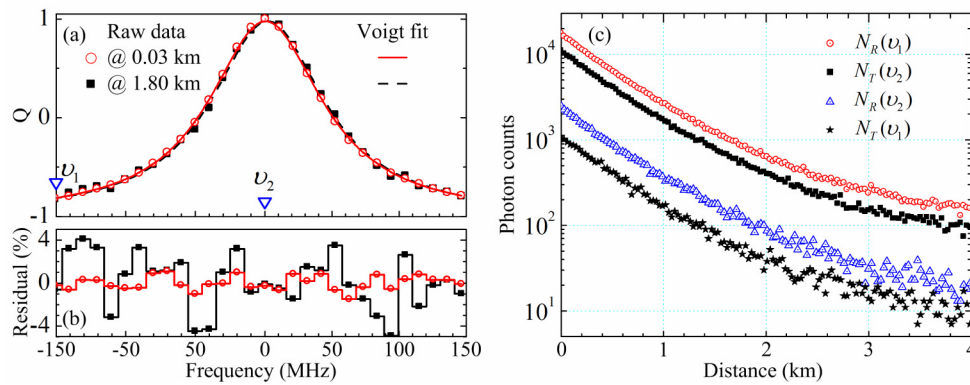


Fig. 7. (a): Frequency response functions of the backscatter aerosol at 0.03 km (open circle) and 1.80 km (filled squares) and their fit results (solid line and dashed line), (b): Residual between the raw frequency response functions and its fit results, (c): Profiles of transmitted and reflected backscatter along distance at given frequencies labeled in Fig. 7(a).

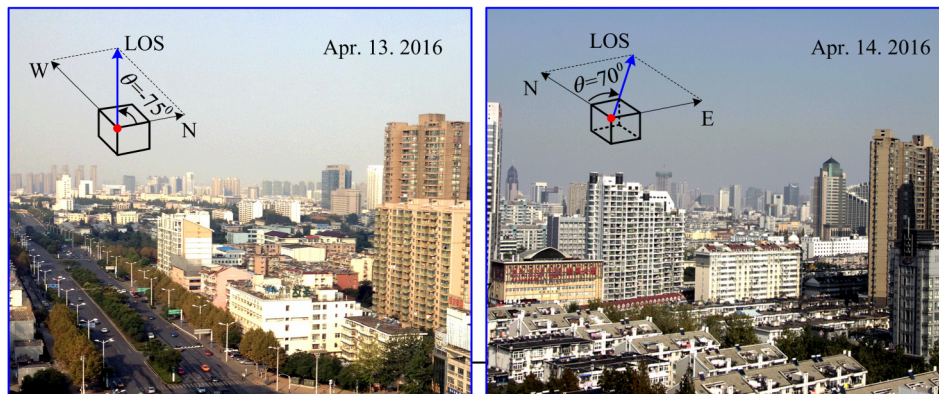


Fig. 8. Photos indicate the pointing of the laser beam

Continuous observations of LOS wind speed are performed from 15:00 PM to 21:00 PM on Apr. 13, 2016 and on Apr. 14, 2016. As indicated in Fig. 8,  $\theta$  is the angle of direction from the north in clockwise. The telescope points at a fixed azimuth angle of  $-75^\circ$  on Apr. 13, 2016, and it points at  $70^\circ$  on Apr. 14, 2016. The wind fields measured are shown in Fig. 9. The distance resolution is switched from 30 m to 60 m at 1.8 km. The time resolution is 1 minute. One interesting phenomenon is that the sign of the wind speed changed at sunset on Apr. 13, 2016. However, the LOS wind speeds show irregular distribution on Apr. 14, 2016. The different observation phenomena between the two consecutive days are relative to the telescope pointing and wind direction. On the first day, the detected region is flat, and the laser beam passed on the top of buildings. However, on the second day, the laser beam passes through the gaps among the buildings, thus the wind field is disrupted.

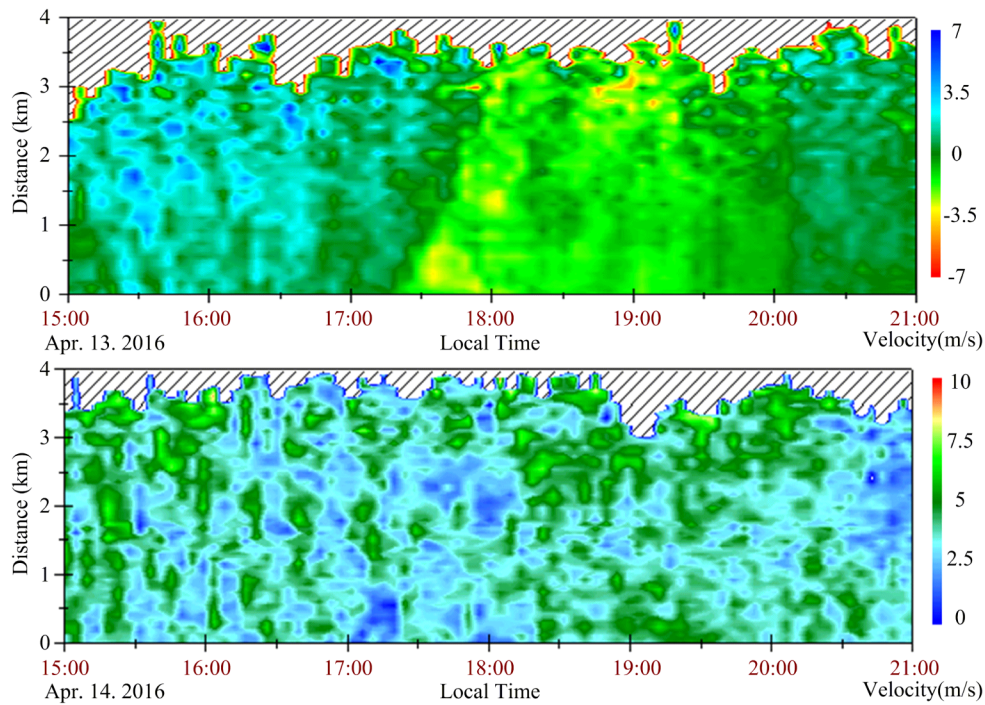


Fig. 9. Time-distance plots of continuous observation of the LOS wind speed using the HSRWL on Apr. 13, 2016 (top) and on Apr. 14, 2016 (bottom).

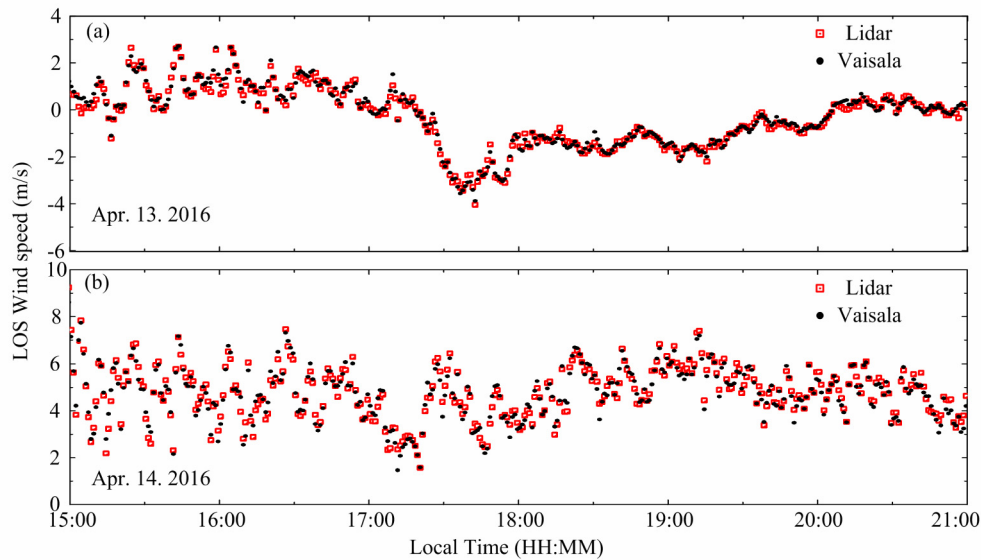


Fig. 10. LOS wind speed measured by the HSRWL (open squares) compared with data measured by the Vaisala windcup (filled circle.) on Apr. 13, 2016 (top) and on Apr. 14, 2016 (bottom).

To estimate the accuracy of the measurements, radial wind velocities from an ultrasonic wind sensor (Vaisala windcap WMT52) are compared with the lidar results in the first bin, as shown in Fig. 10. Two sets of LOS wind speed measurements carried out on Apr. 13 and Apr. 14, 2016 show good agreement.

For quantitative analysis of the correlation of the two sets of the measurements, the scatterplot of the wind components from the HSRWL and the Vaisala windcup is given in Fig. 11(a). The R-square and slope of the linear fit are 0.996 and 0.991 respectively. Figure 11(b) is a histogram distribution of the wind difference between the results from two instruments. The mean difference and the standard deviation of LOS wind speed are 0.01 m/s and 0.50 m/s respectively.

One of the attractive functionalities of the proposed lidar is that not only the Doppler shift but also the bandwidth of the aerosol spectrum can be retrieved simultaneously. Typical profiles of the LOS wind speed and the bandwidth variation are plotted in Figs. 12(a) and 12(c) respectively.

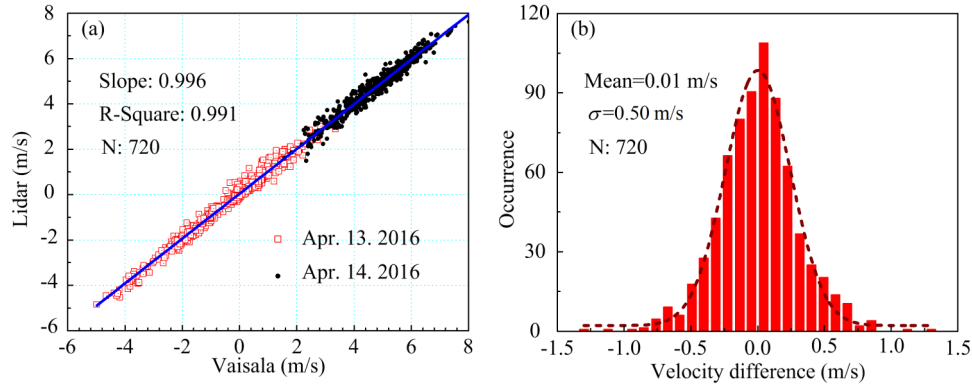


Fig. 11. (a): Scatterplot of wind speed from the HSRWL and Vaisala windcup, (b): Histogram distributions of the velocity difference between the two measurements (red line is the Gaussian fit result to the data).

As shown in Eq. (2) and Eq. (6),  $T(v)$  function and  $R(v)$  function are the Voigt functions, as a result of the convolution of a Gaussian function and a Lorentzian function. Due to the complex expression of the convolution, it is difficult to give an analytic expression of the errors of the wind speed and the bandwidth variation. Thus, an empirical estimation is adopted. As an example, 30 continuous wind profiles and bandwidth variation from 18:00 to 18:30 on Apr. 13, 2016 are selected, since the wind field is relatively stable during short period, as shown in Fig. 9. Then a subtraction of two adjacent profiles is performed, and the results are plotted as circles in Figs. 12(b) and 12(d). The means of the difference at different distance are plotted as yellow line, and the standard deviations of the subtraction ( $\sigma_-$ ) are plotted as red line in Figs. 12(b) and 12(d).

In probability theory, if  $X$  and  $Y$  are independent random variables that are normally distributed, then their difference is also normally distributed. And the square of the standard deviation of their difference is the sum of the square of the two standard deviations, i.e.

$$\sigma^2(X-Y) = \sigma^2(X) + \sigma^2(Y). \quad (8)$$

Assuming the adjacent measurements are independent, then the standard deviation of the measurements  $\sigma_m$  can be described as:

$$\sigma_m = \sigma_- / \sqrt{2}. \quad (9)$$

In Fig. 12, one can see that, the standard deviation of the wind speed is 0.76 m/s at 1.8 km. And the standard deviation of the retrieved bandwidth variation is 2.07 MHz at 1.8 km.

To show the difference of the bandwidth variation between two days, the bandwidth variations from 0 m to 480 m are analyzed statistically. The mean and standard deviation of the bandwidth variation are 2.73 MHz and 2.55 MHz on Apr. 13, 2016. And, the mean and standard deviation of the bandwidth variation are 3.03 MHz and 2.94 MHz on Apr. 14, 2016

(see Fig. 13). The bandwidth variation is directly related to the atmospheric turbulence, and can be used to estimate turbulence energy dissipation rate (TEDR) [4], which is beyond the scope of this article.

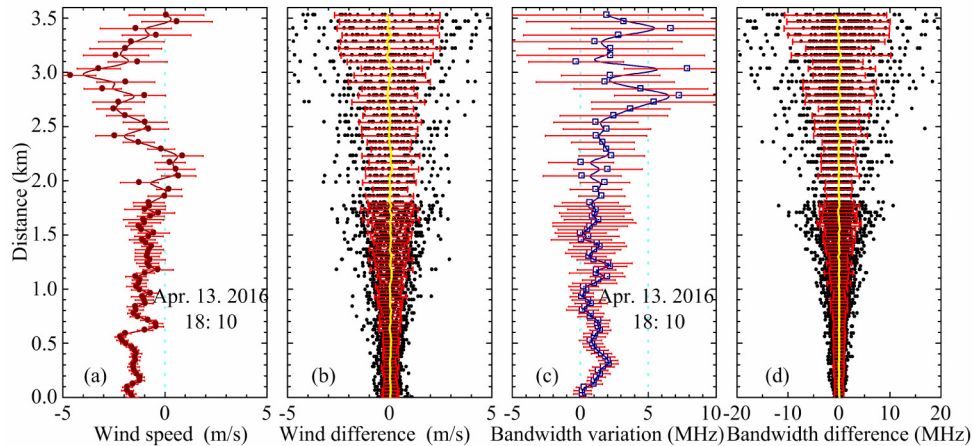


Fig. 12. Profiles of the LOS wind speed (a) and bandwidth variation (c), and the estimated error (b and d).

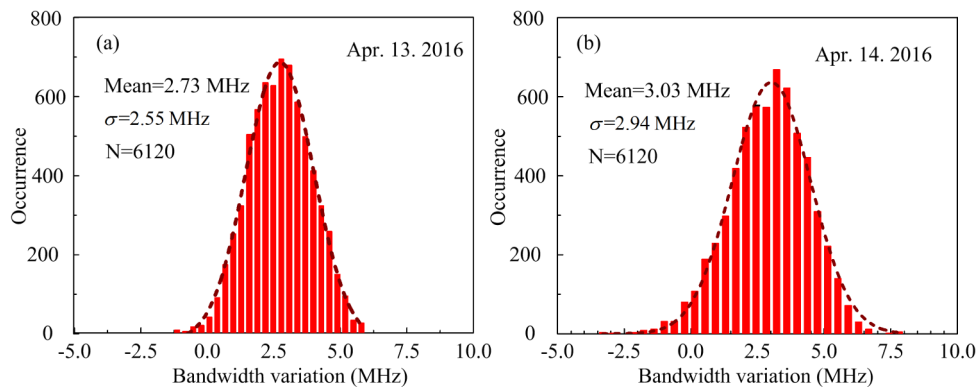


Fig. 13. Statistics of the bandwidth variation: histogram distributions of bandwidth variation from 0 m to 480 m on Apr. 13, 2016(a) and on Apr. 14, 2016(b), solid lines are the Gaussian fit results to the data.

## 5. Conclusion and future research

An all-fiber, eye-safe and micro-pulse direct detection Doppler lidar has been demonstrated by using a high spectral resolution FFP-SI and two high signal-to-noise upconversion detectors. In experiments, a closed-loop temperature controller was adopted, which ensures temperature stability within  $\pm 0.001$  °C during the scanning. Then the effect of thermal fluctuations on the FFP-SI was ignorable. Through spectral analyses of the backscatter signal and reference laser pulse, the Doppler shift and bandwidth variation was retrieved simultaneously. Continuous observation of LOS wind speed was performed. In the comparison experiments, the LOS wind measurements from the HSRWL and the Vaisala windcup were in good agreements. Statistics analysis of the FWHM variation was carried out when the telescope pointed to different directions. In the future research, a matching azimuth-over-elevation scanner will be installed to realize full sky pointing. And the bandwidth variation will be used to study the atmospheric turbulence. In the meantime, the high

temporal and spatial resolution wind data shows great potential in many applications, including measurement of aircraft wake vortices, wind shear, microbursts.

### **Funding**

This work was supported by National Natural Science Foundation (41274151, 41421063); National Fundamental Research Program (2011CB921300, 2013CB336800); CAS Hundred Talents Program (D); CAS Program (KZZD-EW-01-1) and the 10000-Plan of Shandong Province; the Fundamental Research Funds for the Central Universities (WK6030000043).

### **Acknowledgments**

We appreciate the reviewers for their constructive comments. We also thank Dr. Mingyang Zheng and Dr. Xiuping Xie for their help in manufacturing the upconversion detectors.